ARTICLES SCIENCE CHINA Materials

mater.scichina.com link.springer.com

Published online 8 October 2018 | https://doi.org/10.1007/s40843-018-9342-0

Sci China Mater 2019, 62(4): 474–486

Rapid microwave-assisted refluxing synthesis of hierarchical mulberry-shaped $Na_3V_2(PO_4)_2O_2F$@C as high performance cathode for sodium & lithium-ion batteries

Yan Hou[1,2], Kun Chang[3], Zhenyu Wang[2], Shuai Gu[2], Qiong Liu[2], Junjun Zhang[2], Hua Cheng[2], Shenglin Zhang[1], Zhaorong Chang[1*] and Zhouguang Lu[2*]

ABSTRACT **Unique hierarchical mulberry-shaped $Na_3V_2(PO_4)_2O_2F$@C nanocomposite was fabricated by a rapid microwave-assisted low-temperature refluxing strategy. The $V(acac)_3$ reverse micelle systems in the water-in-oil microemulsions played key roles in forming the self-assembly architectures. The prepared $Na_3V_2(PO_4)_2O_2F$@C nanoparticles with the anisotropic growth along the [002] direction were *in-situ* encapsulated in carbon shells, which greatly contribute to fast Na^+/e^- transfer in electrodes. And the self-assemblies with high structure stability help to improve the cycle performance and mitigate voltage fading. The initial discharge capacity of $Na_3V_2(PO_4)_2O_2F$@C as cathode for sodium ion batteries is about 127.9 mA h g^{-1} at 0.1 C. Besides, a high rate performance with a capacity of 88.1 mA h g^{-1} at 20 C has been achieved, and the capacity retains 82.1% after 2,000 cycles. In addition, the reaction kinetics and Na^+ transportation mechanism of $Na_3V_2(PO_4)_2O_2F$@C were preliminarily investigated by the *ex situ* X-ray diffraction, X-ray photoelectron spectroscopy and galvanostatic intermittent titration technique. More interestingly, when coupled with Li, the fabricated hybrid Li/Na-ion batteries also exhibit excellent rate and cycling performances. The proposed rapid refluxing strategy to synthesize mulberry-shaped $Na_3V_2(PO_4)_2O_2F$@C opens up a new opportunity to develop high-performance electrode materials for the energy storage systems.**

Keywords: sodium and lithium ion batteries, cathode materials, fluorophosphates, microwave-assisted refluxing, hierarchical self-assembly

INTRODUCTION

For large-scale storage system, the main parameters of the cells are price, lifetime and power. Since sodium ion batteries (SIBs) are able to satisfy these criteria for the abundance of Na and the far-reachingly analogous intercalation chemistry when compared to their lithium counterparts, the new material families now concern a large part of the scientific community [1]. Among the many cathode materials available for SIBs, such as layered oxides, polyanion-type compounds, metal hexacyanometalates, and organic compounds, polyanion-type compounds are perceived as one promising alternative for future SIBs on account of their structural stability, safety, and appropriate operating potential [2,3]. In comparison with 2D oxide systems, the robust 3D framework of polyanion compounds can offer significant advantages in terms of very stable frameworks, superior thermal-abuse tolerance, and higher output voltage [4–6].

Fluorophosphates should be the most promising candidate for SIBs, because F^- introduction in the phosphate framework can effectively boost the voltage due to the enhanced ionicity of the anionic frame-work [7]. Recently, a variety of fluorophosphates have been reported as Na-ion battery cathode materials, such as Na_2FePO_4F [8–10], $NaVPO_4F$ [11,12], and $Na_3V_2O_{2x}(PO_4)_2F_{3-2x}$ [13–16]. Among these promising cathode materials, sodium-vanadium fluorophosphates are outstanding due to their high energy densities (>500 W h kg^{-1}) [17]. In the $Na_3V_2O_{2x}(PO_4)_2F_{3-2x}$ ($0 \le x \le 1$) series, $Na_3V_2(PO_4)_2O_2F$

[1] Collaborative Innovation Center of Henan Province for Green Manufacturing of Fine Chemicals, School of Chemistry and Chemical Engineering, Henan Normal University, Xinxiang 453007, China
[2] Department of Materials Science & Engineering, Southern University of Science and Technology, Shenzhen 518055, China
[3] National Institute for Materials Science (NIMS), 1-1 Namiki, Tsukuba, Ibaraki 305-0044, Japan
* Corresponding authors (emails: luzg@sustc.edu.cn (Lu Z); czr_56@163.com (Chang Z))

(x=1) should be a better choice than others for the better kinetics for Na transportation with the minimum F content [18,19].

Since the first report of $Na_{1.5}VOPO_4F_{0.5}$ in SIBs by Baudrin and co-workers [20], dramatically increasing attention has been attracted by this high voltage cathode. To optimize the morphology and further improve the electronic conductivity and structural stability of $Na_3V_2(PO_4)_2O_2F$, various synthetic strategies have been attempted. For instance, Guo *et al.* [21] synthesized $Na_3V_2(PO_4)_2O_2F$ nano-tetraprisms using a hydrothermal method (170°C for 12 h). Shen *et al.* [22] fabricated oriented arrays of $Na_3(VO)_2(PO_4)_2F$ cathode using a two-step solvothermal method (170°C for 3 h and 180°C for 6 h) followed by high temperature annealing (400°C for 20 min). Cao *et al.* [23] synthesized 3D architecture $Na_3V_2(PO_4)_2O_2F$@carbon/graphene by a solvothermal method (180°C for 24 h) followed by high temperature annealing (550°C for 1 h). Numerous studies of $Na_3V_2(PO_4)_2O_2F$ cathodes along with their synthesis methods are listed in Table S1. Usually, the reported preparation methods of $Na_3V_2(PO_4)_2O_2F$ materials were involved in the usage of hydrothermal/solvothermal reaction with long time and/or high-temperature calcination to improve the crystallinity. However, such approaches simultaneously caused an increase of the particle size, leading to unsatisfied conductivity of the cathode materials. In this regard, a rapid and facile preparation of porous $Na_3V_2(PO_4)_2O_2F$ with stable morphology and good electronic conductivity, is highly desirable.

Herein, we explore a rapid microwave-assisted low-temperature refluxing strategy for the fabrication of the NASICON-type $Na_3V_2(PO_4)_2O_2F$@C (NVPF@C) with unique hierarchical mulberry-shaped self-assembly architecture for the first time. This novel approach employs a facile low-temperature refluxing process, in which the reverse micelles of vanadium (III) acetylacetonate can take shape from a water-in-tetraethylene glycol emulsion system. These reverse micelles are used as water-insoluble templates for the chemical transformation into $Na_3V_2(PO_4)_2O_2F$ nanocrystals. Subsequently, these crystal nuclei grow and self-assemble into a hierarchical mulberry-like architecture under the inducing and spatial confinement effects of the reverse micellers. In particular, the anisotropic growth of $Na_3V_2(PO_4)_2O_2F$ along the [002] direction facilitates ultrafast Na/Li ion transportation. Furthermore, the acetylacetonate groups were carbonized and *in-situ* coated onto the surface of $Na_3V_2(PO_4)_2O_2F$ to form a conductive layer during the following microwave-assisted solvothermal process. The resultant materials can take advantage of the nanosized primary particles to reduce the Na^+/Li^+ migration pathway and further contribute to favorable kinetics and high capacities, endowing the cathode with high-power performance. Besides, the well-designed self-assemblies with high structural stability also help to improve the cycle performance and mitigate voltage fading. Considering the facile and rapid fabrication of hierarchical carbon-coating nanocomposites, this method could be extended to prepare other high-performance electrode materials in the energy storage field.

EXPERIMENTAL SECTION

Synthesis of $Na_3V_2(PO_4)_2O_2F$@C

All chemicals used were analytical grade without further purification. In a typical procedure, vanadium (III) acetylacetonate ($V(acac)_3$, 0.7181 g), ammonium dihydrogen phosphate ($NH_4H_2PO_4$, 0.2324 g), and sodium fluoride (NaF, 0.1320 g) were separately dissolved in distilled water. Subsequently, the prepared solutions were in turn slowly added to tetraethylene glycol (TEG, 60 mL) under continuous stirring in a three-necked flask. The final volume ratio of TEG/H_2O in the reaction solution was 5:1. The mixture was refluxed at 120°C for 1 h before transferred into 100 mL PTFE/TFM vessels, which were equipped with a temperature probe placed inside a thermowell to monitor the internal temperature of the vessel. The solvothermal reaction was performed with a microwave digestion system (WX-6000, Preekem). For the synthesis, the sample temperature was kept at 220°C for 10 min, followed by natural cooling to ambient temperature. Finally, dark brown precipitation, denoted as NVPF@C, was collected by centrifugation and washed with ethanol several times. Then the obtained sample was dried in a vacuum oven at 80°C overnight. For comparison, $Na_3V_2(PO_4)_2O_2F$ powder (NVPF) was prepared in the absence of the microwave digestion process while keeping other conditions constant.

Physicochemical characterization

Powder X-ray diffraction (XRD) pattern was recorded on a D/Max Ⅲ X-ray diffractometer using Cu Kα radiation (λ = 1.5418 Å) in the scan range (2θ) of 10–120°. X-ray photoelectron spectroscopy (XPS) studies were performed on AXIS Ultra DLD system. Fourier transform infrared spectroscopy (FTIR) measurements were implemented on an IR spectrometer (PerkinElmer, Spectrum One) at room temperature. The morphology,

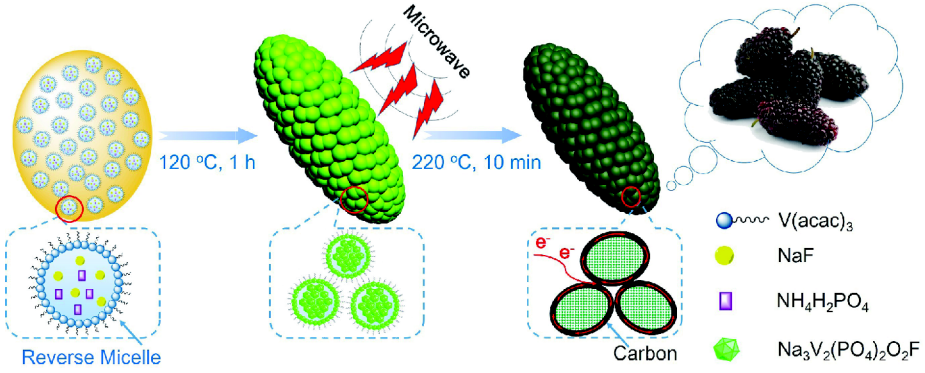

Figure 1 Schematic illustration of the strategy for the fabrication of the mulberry-shaped $Na_3V_2(PO_4)_2O_2F$@C self-assembly nanocomposite.

composition and particle size were investigated by field emission scanning electron microscopy (FESEM, Hitachi S-4800). The images of transmission electron microscopy (TEM) and selected area electron diffraction (SAED) were collected on the JEOL-FEI Jecnai F30. The specific surface area was calculated by the Brumauer-Emmett-Teller (BET) method. The pore size distributions and pore volumes were derived from the adsorption branches of the isotherms by the Barrett–Joyner–Halenda (BJH) model. Raman spectra of samples were obtained on a Lab RAM HR 800 Raman microscope with an excitation laser beam of 532 nm wavelength. Thermogravimetry-differential scanning calorimetry (TG-DSC) analyses of NVPF@C were performed on a Netzsch STA 409 PC/PG thermogravimetric analyzer.

Electrochemical measurement

The electrochemical measurements were performed at room temperature with CR2025 coin cells assembled in an argon-filled glove box. To form the working electrode, a carbon-coated composite material (NVPF@C) was mixed with conductive carbon black (Timcal Super-P) and carboxymethylcellulose (CMC) in 80:10:10 ratio, respectively. The mixture was blended with deionized water [24]. The resulting slurry was applied on Al foil with the "doctor blade" technique and then dried at 60°C for 1 h. Dried electrodes were rolled, punched to round discs, and dried at 60°C for 12 h under dynamic vacuum. The loading density of active material on the work electrodes is about 2.5–3.0 mg cm^{-2}. Electrolyte was 1 mol L^{-1} $NaClO_4$ dissolved in ethylene carbonate (EC) and propylene carbonate (PC) (1:1 by volume). Metallic Na and Li were used as negative electrodes in the Na-ion and the hybrid Li/Na batteries, respectively. Galvanostatic charge/discharge tests were carried out on Neware battery test systems (Shengzhen, China) in the potential windows of 2.0–4.3 V *vs.* Na^+/Na and 2.5–4.5 V *vs.* Li^+/Li. Galvanostatic intermittent titration technique (GITT) analyses, cyclic voltammetry (CV) tests and electrochemical impedance spectra (EIS) were carried out using an IM6ex electrochemistry workstation (Zahner-Elektrick, German). CV curves were collected at the varied scan rates from 0.1 to 1 mV s^{-1}. The EIS were measured in the frequency range from 1 MHz to 1 mHz. For GITT analyses, the cells were cycled in the potential window of 2.0–4.3 V *vs.* Na^+/Na^+ at a rate of 0.05 C. The duration time for each applied galvanostatic current and rest was 1 and 6 h, respectively. *Ex-situ* XRD and XPS studies were carried out to examine the Na insertion/extraction mechanism.

RESULTS AND DISCUSSION

The synthetic procedure of $Na_3V_2(PO_4)_2O_2F$@C is schematically displayed in Fig. 1. In the refluxing process, V(acac)$_3$ solution was firstly dissolved in TEG, generating numerous reverse micelles in the water-in-oil microemulsions. For reverse micelles, the surfactant molecules formed layers at the oil/water interface, with the hydrophobic tails of the surfactant molecules dissolved in the external oil phase and the hydrophilic head groups in the internal aqueous phase [25,26]. The growth of $Na_3V_2(PO_4)_2O_2F$ cluster nucleation took place upon fast exchange of the liquid content of the surfactant-stabilized micellar pools, in which precursors of $NH_4H_2PO_4$ and NaF have previously been dissolved. Particularly, oxygen was involved in this reaction, which means that V^{3+} in the droplet should diffuse to the surface and be oxidized to form V^{4+} when exposed to air. In the V(acac)$_3$ reverse micelle systems, the ion-transportation could occur through collision between microdroplets that carry dif-

ferent reactants with their aqueous cores. Then $Na_3V_2(PO_4)_2O_2F$ crystal nuclei formed on the inner surface of the reverse micelle upon local supersaturation. Subsequently, the crystal nuclei grew and assembled into a mulberry-like morphology under the induction and spatial confinement effects of the reverse micellers. During the reluxing process, the micelle biomimetic system, similar to vesicles, formed a relatively stable and confined nanoscaled environment for the growth and assembly of $Na_3V_2(PO_4)_2O_2F$. The polyol medium itself also acted as a stabilizer, limiting the growth and prohibiting agglomeration of the obtained particles. These $Na_3V_2(PO_4)_2O_2F$ nanoparticles could subsequently be coated with carbon *via* a microwave-driven carbonization process, ultimately affording excellent charge cyclability and rate performance as cathode in Na^+/Li^+ storage batteries [27]. The microwave-assisted low-temperature synthesis strategy dramatically reduced processing time, increased product yields, and enhanced product purity compared to conventionally processed experiments [26]. Simultaneously, as the carbon and vanadium were derived from the single-component precursor $V(acac)_3$, undesired particle growth was effectively suppressed during the microwave assisted solvothermal process, resulting in small nanocrystalline $Na_3V_2(PO_4)_2O_2F$ particles with a uniform carbon shell. The optimized design of the hierarchical mulberry-shaped self-assembly architecture endows $Na_3V_2(PO_4)_2O_2F$@C with the effective ambipolar diffusion of Na^+/Li^+ and e^- into and out of the electrode, which is expected to provide outstanding electrochemical performance in Na^+/Li^+ cells.

Time-dependent experiments were performed to gain insight into the formation process of NVPF@C. Products were collected at different stages of the reaction system, and their morphologies were subjected to SEM and TEM investigation. As shown in Fig. 2a, the sample collected immediately after its formation (t=0) is comprised of irregular nanoparticles smaller than 30 nm in diameter;

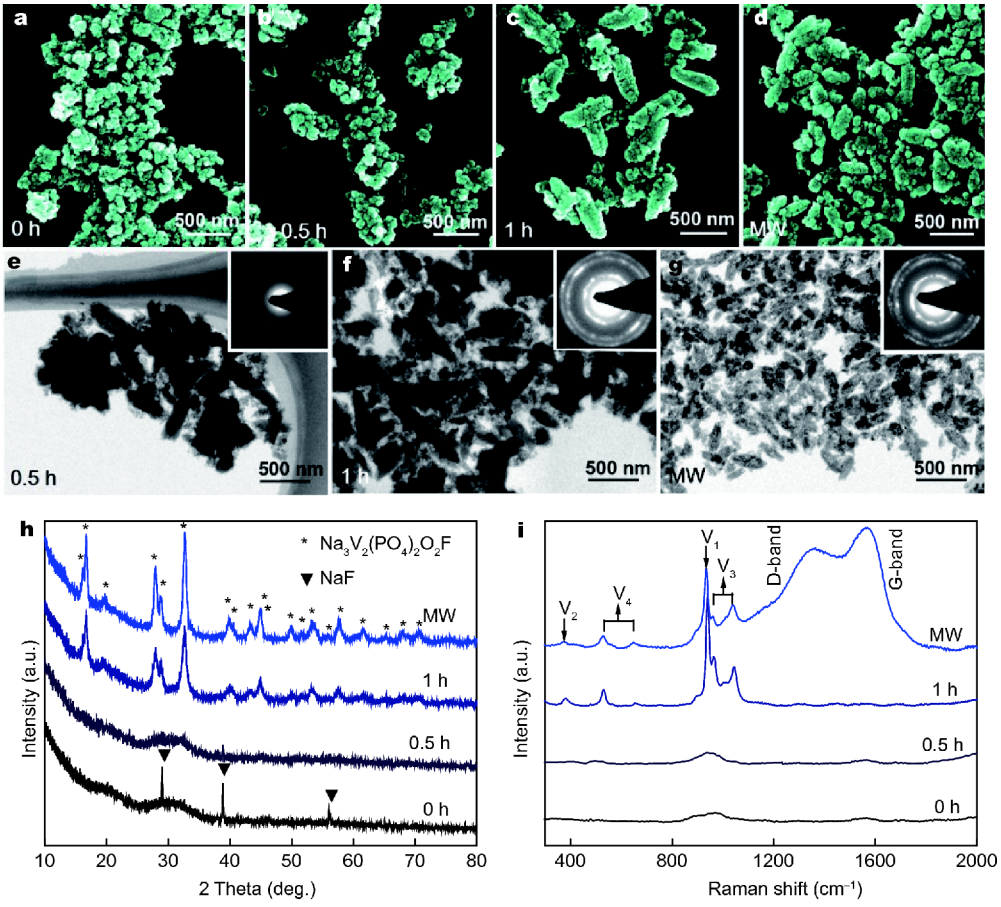

Figure 2 SEM and TEM images of the samples collected from the reaction solution at various growth stage: (a) 0 h, (b) and (e) 0.5 h, (c) and (f) 1 h; (d) and (g) 220°C for 10 min of the microwave-assisted solvothermal process. Evolution of XRD (h) and Raman (i) patterns of the samples at various growth stage.

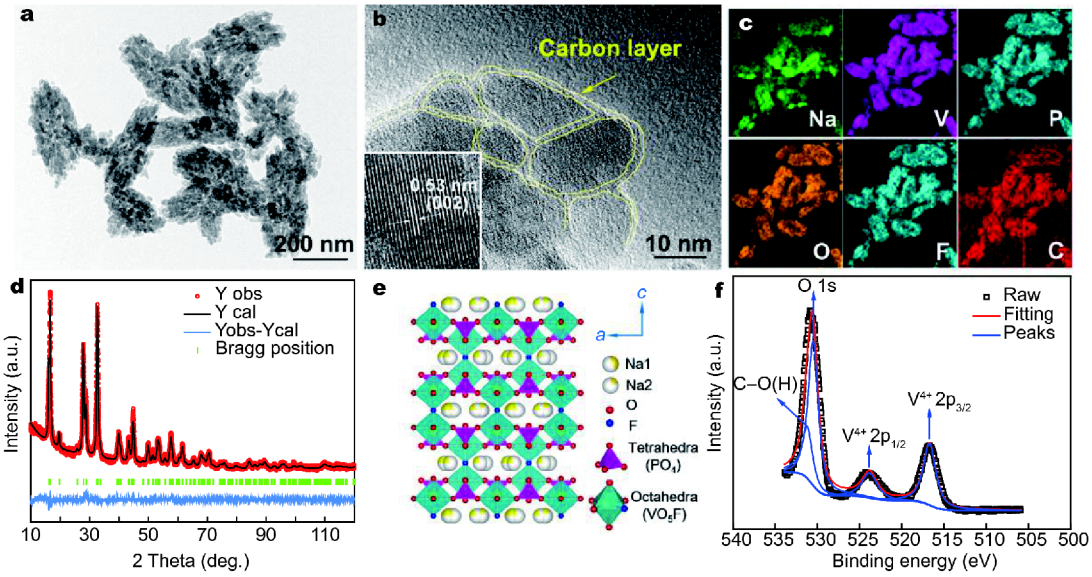

Figure 3 Morphological and structural characterizations of NVPF@C. (a) TEM image; (b) HRTEM image; (c) EDX elemental mapping; (d) powder X-ray diffraction pattern and Rietveld refinements; (e) crystal structure of the $Na_3V_2(PO_4)_2O_2F$; (f) high resolution XPS spectra of V 2p.

after 0.5 h, the nanoparticles grew up and tended to self-assemble gradually (Fig. 2b, e). The mulberry-shaped nanoparticles formed over the following 0.5 h (Fig. 2c, f), which were very stable in solution and their highly ordered superstructure remained unchanged in the subsequent microwave-assisted solvothermal process (Fig. 2d, g). After the microwave radiation, the nanoparticles shrunk significantly, and became more uniform in size than that before the radiation treatment. It is noted that serious aggregation appeared when the reaction time was prolonged to 3.5 h (Fig. S1a).

With the morphology of the samples continually evolved during reaction, the composition also changed, as confirmed by XRD and Raman analysis. As shown in Fig. 2h, the XRD pattern with characteristic peaks at around 29.1°, 38.8° and 56.0° is detected for NaF when t=0; after 0.5 h, the collected products were amorphous. Highly crystallized $Na_3V_2(PO_4)_2O_2F$ was observed when the reaction time was extended to 1 h (Fig. S2). The enhanced intensity of characteristic peaks and the marked selected area electron diffraction (SAED) rings (insets of Fig. 2e and f) show the improved crystallinity with the extension of the refluxing time. Moreover, prolonging the reaction time to 3 h caused the intrusion of $Na_3V_2(PO_4)_3$ impurity (Fig. S1b). Raman spectra (Fig. 2i) of the collected products also show that crystallized $Na_3V_2(PO_4)_2O_2F$ was observed when the reaction time was extended to 1 h. The peaks of the products NVPF (collected from liquid-phase reaction solution at 120°C for 1 h) at 940, 1,040, and 377 cm^{-1} are assigned to v_1, v_3, and v_2 modes of the PO_4^{3-} anion, respectively [8,28]. There are no obvious peaks for ordered and disordered carbon in the range of 1,300 to 1,700 cm^{-1}. In contrast, it is noticed that the Raman scattering peak of PO_4^{3-} in NVPF@C (collected after microwave-assisted solvothermal treatment at 220°C for 10 min) was weaker than that of NVPF. Moreover, the existence of carbon in NVPF@C was detected by Raman spectra (the top curve in Fig. 2i). The broad peak at 1,350 cm^{-1} (D-band) is attributed to the sp^3 C and 1,580 cm^{-1} (G-band) is due to the vibration of sp^2 C in the graphitic structure; the existence of both D and G bands suggests that the formed carbon layer consists of disordered carbon with small graphitic domains [29].

According to the procedure described in the Experimental Section, NVPF@C powder was obtained. TEM observation is performed to confirm the detailed internal microstructure of the as-prepared NVPF@C. It can be seen from Fig. 3a that the NVPF@C samples exhibit a mulberry-shaped morphology with an average length of ~220 nm and ~100 nm in center width. Careful examination (Fig. S3) further reveals that these mulberry-shaped nanoparticles are constructed from ~25-nm-sized crystallites. This signifies exceptionally short transportation lengths for both electrons and ions, resulting in fast charge-discharge transfer kinetics. Furthermore, nanoscaled materials possessing high surface area and short diffusion paths could offer more electrochemically active sites, mitigate the concentration polarization of electrode

materials, and accommodate the strain of Na intercalation/deintercalation [30]. A high-magnification TEM image (Fig. 3b) reveals that a thin carbon layer (approximately 1–2 nm thick) has been obtained from the carbonization of organic macromolecular residues that coated on the crystallite to form a NVPF@C core-shell structure. Na^+/Li^+ can easily pass through the thin carbon shell for the insertion reaction with $Na_3V_2(PO4)_2O_2F$ which is accompanied by the accepted electrons. Moreover, $Na_3V_2(PO4)_2O_2F$ crystallites are connected with each other through the carbon shell, thereby ensuring electrical continuity around the crystallites and hence improving the cycle capacity and rate performance. The carbon content of the prepared NVPF@C composite is measured using thermogravimetric analysis and made up ~2.5 wt% of the specimen (Fig. S4). The observed lattice spacing value is 0.53 nm, corresponding well with the (002) facet, which is in accordance with the XRD results. The anisotropic growth of $Na_3V_2(PO_4)_2O_2F$ along the [002] direction improves fast Na ion insertion/extraction [22]. Energy-dispersive X-ray (EDX) elemental mapping for the sample in Fig. 3c shows the uniform distribution of Na, V, O, P, F and C.

The pore size distribution and surface area (Fig. S5) were calculated by the BJH model and the BET method, respectively. The sample NVPF@C shows a typical type-IV nitrogen adsorption–desorption isotherm. The BET surface area of the NVPF@C is calculated to be 89 $m^2 g^{-1}$. The main pore structure consists of mesopores (centered at 6.1 nm) and micropores (centered at 1.9 nm), which gives rise to a high pore volume (0.5 $cm^3 g^{-1}$). The mesopores may be derived from the accumulation of different NVPF@C nanoparticles, while the micropores are attributed to the inter grain packing inside the NVPF@C nanoparticles, which is expected to enable sufficient wetting with the electrolyte [31].

Fig. 3d shows the powder XRD pattern and rietveld refinement result of the as-prepared material, which indicates that this sample adopts tetragonal *I*4/*mmm* space group with lattice parameters $a=b=6.3816$ Å and $c=10.6125$ Å. The result is consistent with the No. 411950 (tetragonal $Na_3V_2(PO_4)_2O_2F$) data in the Inorganic Crystal Structure Database [32]. Particularly, the result also shows the reasonably small agreement factors with $R_p=4.78\%$ and $R_{wp}=6.04\%$. The structural parameters are listed in Table S2 in the electronic supplementary information. Fig. 3e shows the crystal structure of $Na_3V_2(PO_4)_2O_2F$, in which the VO_5F octachedrons share O atoms with PO_4 tetrahedrons vertices parallel to the *ab*-plane, forming pseudolayers along the *ab*-plane. These layers are loosely interconnected along the *c*-axis over the F ligands. Between different layers, there is a broad channel which is in favour of rapid Na^+/Li^+ intercalation/extraction during the charge and discharge processes.

XPS was employed to further gain insight into the chemical composition and bonds in NVPF@C. The survey spectrum in Fig. S6 illustrates the presence of Na, V, P, O, F and C elements in the NVPF@C samples. The high-resolution XPS analysis of V 2p (Fig. 3f) shows two characteristic peaks with binding energy of 516.7 eV (V $2p_{3/2}$) and 523.8 eV (V $2p_{1/2}$), indicating the existence of V^{4+} species in NVPF@C samples. This is consistent with previous reports [21,33]. Moreover, the high-resolution of C 1s spectrum in Fig. S7 further confirms the formation of C=C peak at 284.8 eV, indicating the restoration of sp^2 hybridized carbon coating. Additionally, small peaks corresponding to C–O and C=O separately located at 286.6 and 288.5 eV, suggest that the acetylacetone groups of $V(acac)_3$ were nearly completely carbonized.

The FTIR spectrum of the prepared NVPF@C was collected to grasp further information on the vanadium environment, as shown in Fig. S8. The broad band at 1,000–1,150 cm^{-1} can be ascribed to the asymmetric stretching vibration (ν_{as}) of PO_4^{3-} tetrahedrons, and the bands at 673, 558 and 450 cm^{-1} indicate the P–O symmetric stretching, bending and asymmetric stretching vibrations (ν_{ss}, ν_b and ν_{as}), respectively. The peak associated with V–F bonds is at 944 cm^{-1}, while the strong band center at 917 cm^{-1} is attributed to the V=O stretching vibration [20,34].

The hierarchical mulberry-shaped NVPF@C electrode is expected to provide outstanding electrochemical performance in sodium ion cells. In characterizing the electrochemical properties of NVPF@C electrodes, the CV and galvanostatic charge/discharge (GCD) curves were investigated in the coin-type half-cells with a voltage window of 2.5–4.3 V *vs.* Na^+/Na. Firstly, CV was measured at a scan rate of 0.1 mV s^{-1} to identify the activity of the vanadium redox couple. As shown in Fig. 4a, the NVPF@C exhibits two pair of redox peaks located at around 4.06/4.00 and 3.65/3.50 V, which is corresponding to the activity of V^{4+}/V^{5+} couple. It also can be found that the NVPF@C has a smaller polarization than NVPF, reflecting facile electronic and ionic transport kinetics when the $Na_3V_2(PO_4)_2O_2F$ particles were coated by carbon shell. The initial charge-discharge curves of NVPF@C and NVPF cycled at a current density of 0.1 C (1 C corresponds to a current density of 130 mA g^{-1}) are shown in Fig. 4b. The NVPF@C displays an initial discharge spe-

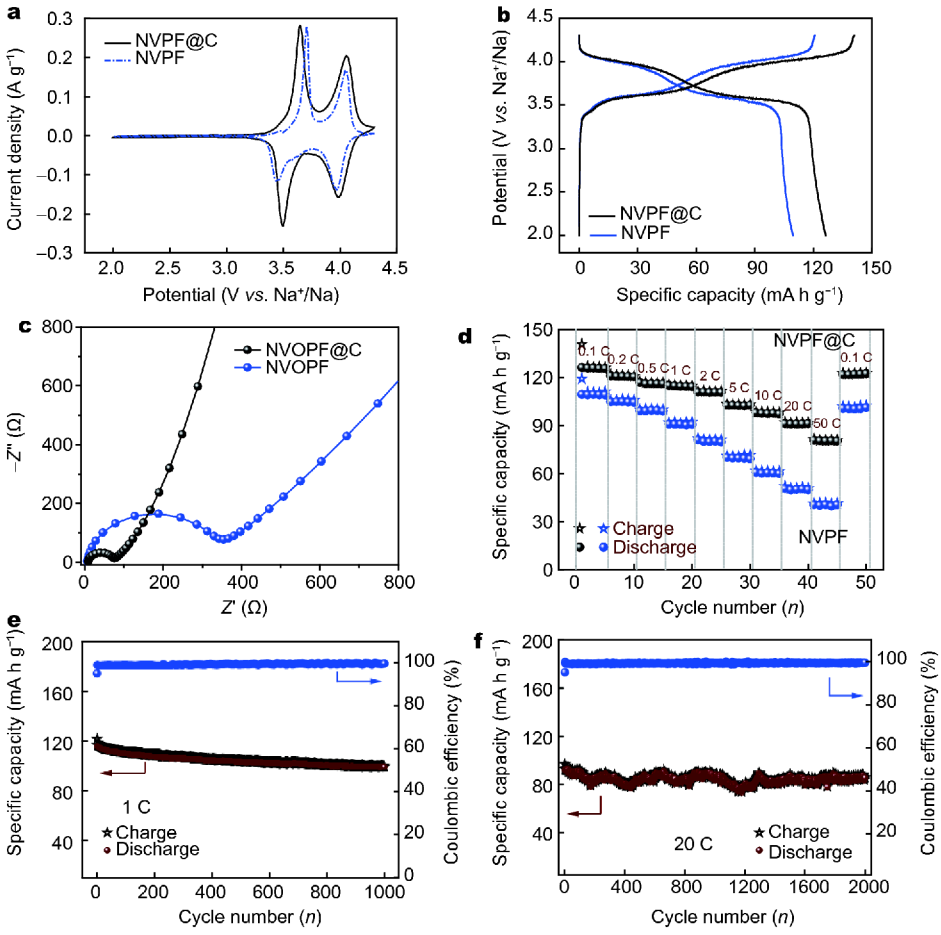

Figure 4 Comparison of the electrochemical performance of the prepared NVPF and NVPF@C (*vs.* Na^+/Na): (a) Representative CV and (b) galvanostatic charge/discharge curves of the initial cycles; (c) Nyquist plots of the impedance spectra; (d) rate capabilities from 0.1 to 50 C; (e) and (f) cycle stabilities at different rates of 1 C for 1,000 cycles and 20 C for 2,000 cycles.

cific capacity of 127.9 mA h g^{-1} (based on the mass of NVPF@C), which is higher than that of NVPF (110.0 mA h g^{-1}). Two plateaus can be observed at ~4.02 V and 3.65 V in the discharge curves, respectively, which agrees well with the potential positions of the CV peaks. Moreover, the NVPF@C exhibits superior rate capacity and excellent cycling stability due to the superior electrode kinetics and low lattice strain during Na^+ intercalation/extraction. The rate performance of NVPF@C and NVPF has been investigated at various charge-discharge current densities from 0.1 to 50 C (Fig. 4d). Obviously, with the increasing current density, the NVPF@C exhibits higher capacity and smaller capacity decay than NVPF. At the current densities of 0.5, 5 and 50 C, the NVPF@C delivers discharge capacity of 117.5, 103.3 and 81.2 mA h g^{-1}, respectively. When the test current returns to the low rate of 0.1 C, the discharge capacity recovers to 122.7 mA h g^{-1}. This value corresponds to a capacity retention of ~96.6%. The GCD curves of NVPF@C at different current densities from 0.1 to 50 C are displayed in Fig. S9, which shows a small polarization. EIS was used to characterize the charge transfer properties of the NVPF@C and NVPF electrodes. Fig. 4c shows that the charge transfer resistance of the NVPF@C is only 74.9 Ω, whereas the resistance for the NVPF electrode increases to 330.1 Ω. The resistance is simulated using the equivalent circuit of $R_b(Q_1R_1)(Q_2(R_2W))$ shown in Fig. S10. The NVPF@C also exhibits outstanding cycling performance at different current densities of 1 and 20 C (Fig. 4e and f). When cycled at 1 C, the NVPF@C delivers an initial capacity of 115.8 mA h g^{-1} and retains up to 89.8% of its capacity after 1,000 cycles. Furthermore, the NVPF@C electrode was cycled at the high current densities of 20 C with about 82.1% retention even after 2,000

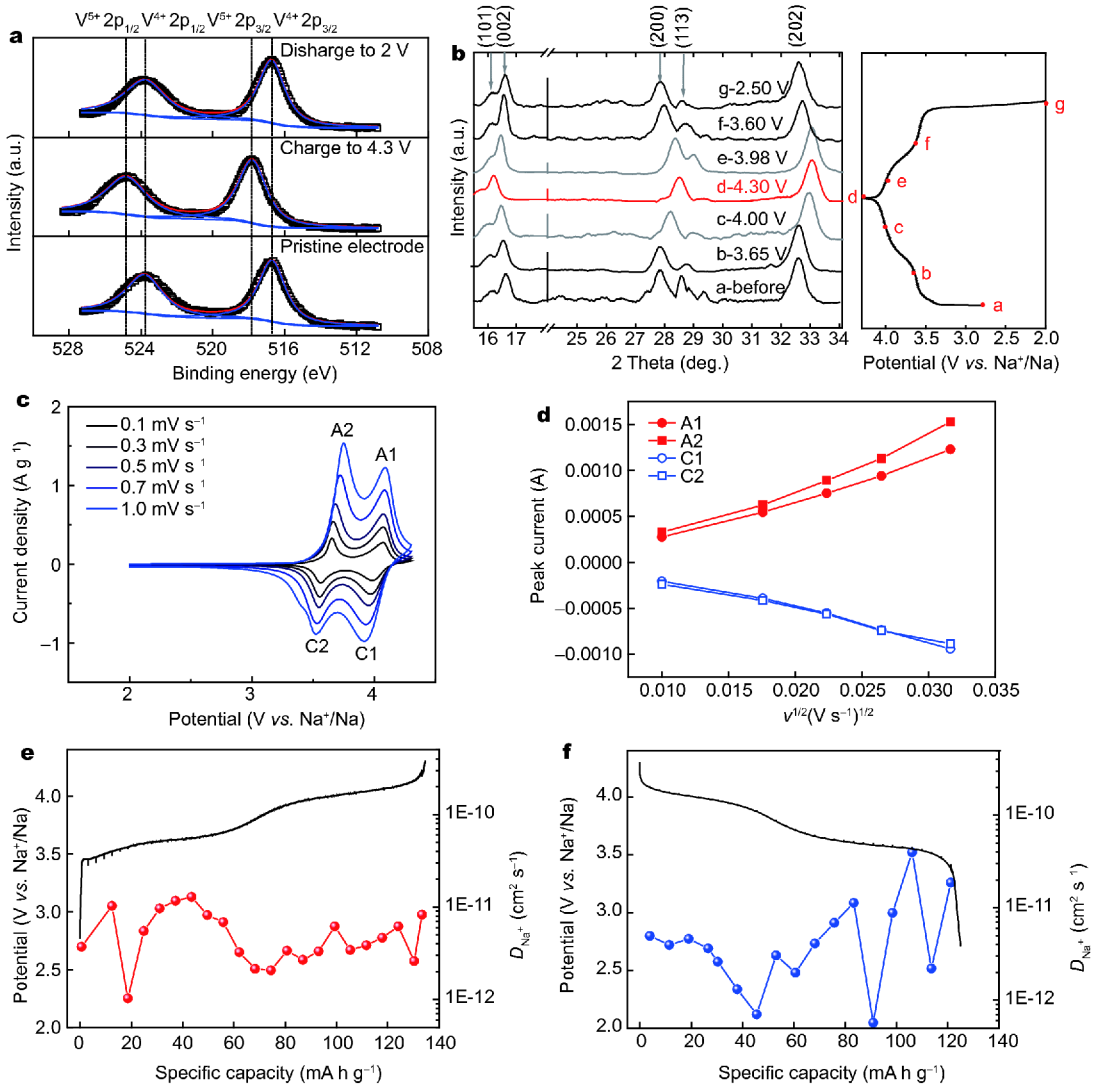

Figure 5 Spectroscopy investigation of the electrochemical reaction mechanism. (a) Comparison of XPS of V element and (b) *ex situ* XRD patterns collected at various charging/discharging states. (c) CV curves of various scan rates; (d) corresponding relationship between the peak current i_p and the square root of the scan rate $v^{1/2}$; GITT curves and the changes of the Na^+ diffusion coefficient of NVPF@C in the initial charge (e) and discharge (f) processes.

cycles. Indeed the scanning electron microscopy (SEM) examination of the electrode material after cycling in Fig. S11 shows that the mulberry-shaped NVPF@C architecture is well preserved without obvious deformation. The rate capability and cycling stability of the NVPF@C electrode exceed that of NVPF, and the main reasons are as follows: (1) *in-situ* carbon shell greatly enhances the electronic conductivity of the material and maintains the stability of structure in the cycling process; (2) with the microwave radiation, the material has been better crystallized, which has a positive effect on improving the ions mobility.

Ex-situ XPS studies were carried out to investigate the electrochemical reaction of the NVPF@C electrode. As shown in Fig. 5a, the pristine electrode displayed two peaks located at the 516.7 and 523.8 eV, corresponding to V^{4+}. Notably, with the extraction of Na^+ and after charged to 4.3 V, the binding energy of V increased significantly to 517.8 and 524.9 eV, indicating the formation of a higher oxidation state, namely V^{5+} [35]. Upon discharge, the V^{5+} species were fully reduced to V^{4+}. The above results proved that the transition from $Na_3V_2(PO_4)_2O_2F$ to $NaV_2(PO_4)_2O_2F$ during the charge process, and then back to $Na_3V_2(PO_4)_2O_2F$ during the discharge process, as shown with the Equations (1) and (2) [36,37]: $Na_3V_2(PO_4)_2O_2F \leftrightarrow Na_xV_2(PO_4)_2O_2F + xNa^+ + xe^-$ ($2 \le x \le 3$) (1) and

$Na_2V_2(PO_4)_2O_2F \leftrightarrow Na_xV_2(PO_4)_2O_2F + xNa^+ + xe^-$ $(1 \leq x \leq 2)$ (2).

Furthermore, *ex situ* XRD technique was performed to provide more insight about the structural change of the NVPF@C electrode during charge/discharge process. Fig. 5b reveals the details of structural evolutions at various charge and discharge states. Overall, a continuous peak shift was observed, implying a widespread solid-solution region. Upon closer observation, the peaks at 27.83° shifted positively during the charging process, indicating that the *d*-space decreases due to the Na ion extraction. At the end of charging, the peaks at 27.83° and 28.60° merged into one peak at 28.52°, which is in good agreement with the XRD pattern of $NaV_2(PO_4)_2O_2F$ (a two-Na-extracted product of $Na_3V_2(PO_4)_2O_2F$) [17,22]. In addition, the two diffraction peaks shifted back to original positions during the discharging process, suggesting structure reversibility, which were also demonstrated by the reversible variations of other peaks at 16.15°, 16.62° and 32.59°. The high reversibility of structure gives rise to excellent cyclability of the NVPF@C cathode for SIBs.

CV at various scan rates and GITT tests were employed to analyze the Na-migration kinetics of the NVPF@C electrode to preliminarily evaluate the possibility of high-rate capabilities. As shown in Fig. 5c, CV curves were recorded at various scan rates from 0.1 to 1 mV s^{-1} to obtain the Na^+ diffusion coefficient (D_{Na^+}) according to the Randles-Sevcik equation [38]. As displayed in Fig. 5d, the good linear relationships for plots of peak current (i_p) *vs.* square root of the scan rate ($v^{1/2}$) demonstrate a diffusion-controlled process of sodium (de)intercalation for NVPF@C. From the slope of the fitting line collected from the peaks of A1, A2, C1 and C2 (Fig. S12), the *D* values of NVPF@C electrode are 6.90×10^{-11}, 8.68×10^{-11}, 5.41×10^{-11} and 4.85×10^{-11} cm^2 s^{-1} for peaks A1, A2, C1 and C2, respectively. Especially, the low-potential A2 yields higher *D* value than the high-potential of A1, suggesting that the Na extraction at a low potential of around 3.7 V is relatively rapid due to the high concentration of Na ions in the electrode in the initial stage of charging. However, the electrode at low-potential of peak C2 yields smaller *D* value than the high-potential of peak C1, suggesting that the Na intercalation at the low potential is relatively sluggish and requires higher energy.

Tests according to the GITT were carried out to further evaluate Na^+ diffusion in the NVPF@C electrode. Fig. 5e and f display the GITT profile of the NVPF@C during the initial charge and discharge process. Fig. S13a shows a typical τ *versus* *E* profile for a single titration. Based on Equation S3, the D_{Na^+} at varied voltages during the whole charge and discharge process could be determined. As shown in Fig. 5e and f, the D_{Na^+} values are in the 10^{-13}–10^{-10} cm^2 s^{-1} order of magnitude, and the values at the lower plateau are slightly higher than those at the higher plateau in both the charge and discharge processes. This finding is consistent with the CV test results. The low points in the profiles located at around 3.55 V correspond well to the potential plateaus in the charge-discharge curves. The minimum ion diffusion coefficient D_{Na^+} values in the central of the plateau region can be ascribed to the strong interactions between the host matrix and the intercalation ions during the $Na_3V_2(PO_4)_2O_2F \leftrightarrow Na_xV_2(PO_4)_2O_2F$ $(2 \leq x \leq 3)$ transition reaction, indicating that it is approaching to the equilibrium state. Such similar phenomena have also been detected in previous reports [21,39]. Notably, the high D_{Na^+} of NVPF@C electrode can be ascribed to the nanoscale size of primary particles, which shortens the ions diffusion paths. In addition, the improved electronic conductivity of NVPF@C is also in favor of enhancing redox kinetics performance.

Similar to $Na_3V_2(PO_4)_3$, $Na_3V_2(PO_4)_2O_2F$ can also be used as sodium-based cathode materials for hybrid Li/Na-ion batteries (HLNIBs) [40,41]. In turn, the electrochemical performance of NVPF@C as cathode for hybrid HLNIBs has also been investigated by CV and GCD tests in a voltage window of 2.5–4.5 V with metallic Li plates as both counter and reference electrodes. Fig. 6a displays the CV curves of the NVPF@C electrode at a scan rate of 0.1 mV s^{-1} over the potential window of 2.5–4.5 V *versus* Li^+/Li. Two couples of anodic/cathodic peaks (4.32/4.19 V and 3.93/3.78 V) of V^{5+}/V^{4+} in NVPF@C can be clearly observed from the CV curves. Notably, the anodic/cathodic peaks' values of the NVPF@C electrode (using the electrolyte with $NaClO_4$ as solute) in this work are higher than that of the previous report [40] (4.22/4.12 V and 3.91/3.80 V) in which $LiPF_6$ was used as solute in electrolyte due to the better conductivity for $NaClO_4$.

GCD tests were implemented to investigate the rate performance of NVPF@C (Fig. 6b, c). The discharge specific capacity of NVPF@C *vs.* Li^+/Li is 118.2 mA h g^{-1} at 0.065 A g^{-1}. Two pairs of oxidation/reduction plateaus are observed at 4.24/4.23 V and 3.84/3.83 V *vs.* Li^+/Li. Similarly to CV, the oxidation/reduction plateaus are also higher than previous report [40] when using $LiPF_6$ as solute in electrolyte. It can still deliver a specific capacity of 85.6 mA h g^{-1} even at a high current density of 2.6 A g^{-1}. When the test current returns to the low current density of 0.065 A g^{-1}, the discharge capacity recovers to 116.3 mA h g^{-1} which corresponds to a capacity

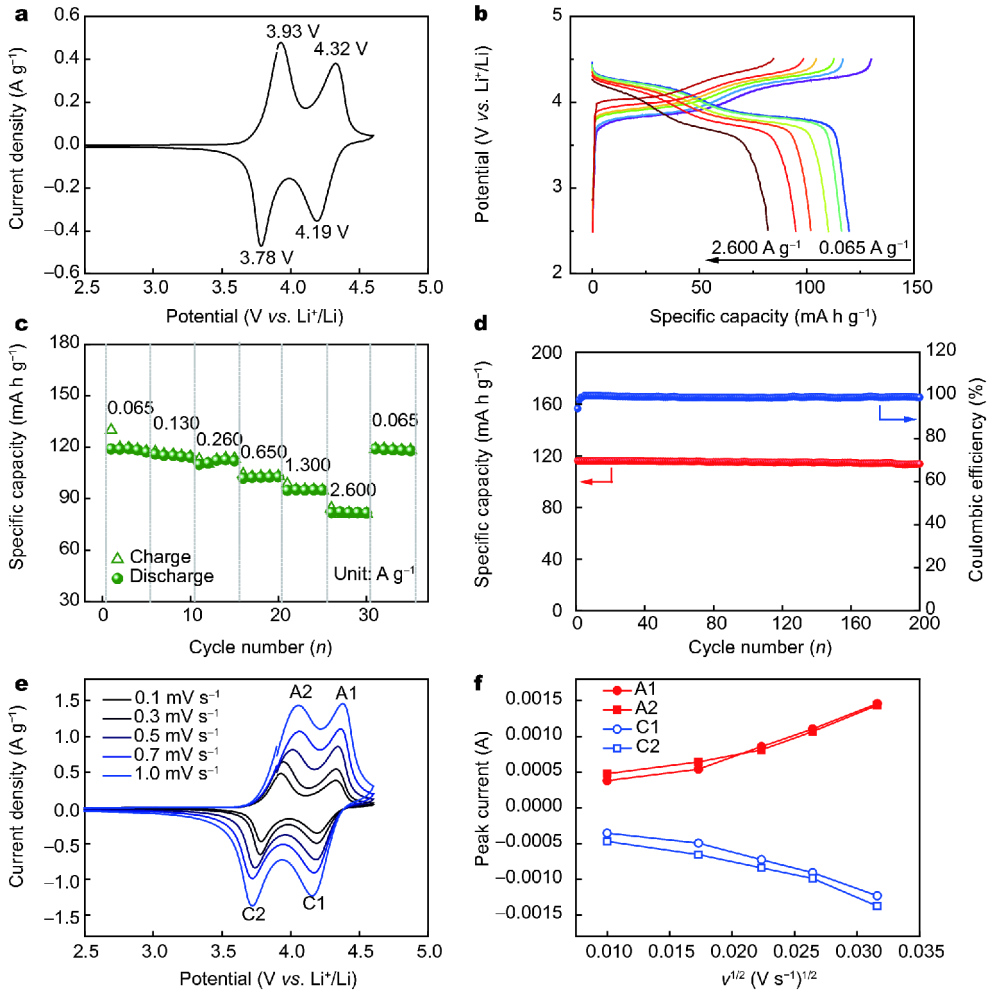

Figure 6 The electrochemical performance of NVPF@C in the potential range from 2.5 to 4.5 V (*vs.* Li^+/Li): (a) CV curve at a scan rate of 0.1 mV s^{-1}; (b) GCD curves and (c) rate performance at various current density from 0.065 to 2.600 A g^{-1}; (d) cycle stabilities at a current density of 0.13 A g^{-1}; (e) CV curves at various scan rates; (f) corresponding relationship between the peak current i_p and the square root of the scan rate $v^{1/2}$.

retention of ~98.3%. Fig. 6d gives its cycling performance at a moderate current density of 0.13 A g^{-1}. The capacity retention is still up to 97.4% after 200 cycles, implying the superior cycling stability of the NVPOF@C electrode for Li storage.

To analyze the reaction kinetics and the mechanism of the NVPF@C electrode during the Na^+/Li^+ de-/intercalation process, CV test was further conducted in the NVPF@C *vs.* Li^+/Li cells. As shown in Fig. 6e, CV curves were recorded at various scan rates from 0.1 to 1 mV s^{-1} to obtain the diffusion coefficient (D_{Na^+/Li^+}) according to Equation S1 (Supporting Information). From the slope of the fitting line collected from the peaks of A1, A2, C1 and C2 (Fig. S14), the D_{Na^+/Li^+} values of NVPF@C electrode are 8.02×10^{-11}, 6.88×10^{-11}, 6.37×10^{-11} and 6.33×10^{-11} cm^2 s^{-1} for peaks A1, A2, C1 and C2, respectively. The D_{Na^+/Li^+} values during the discharge process are higher than those in NVPF@C *vs.* Na^+/Na cells, because the Li^+ intercalation into $Na_3V_2(PO_4)_2O_2F$ materials is easier than Na^+ [42].

Numerous studies of $Na_3V_2(PO_4)_2O_2F$ cathodes along with their capacity values are listed in Table S1. Apparently, our results display one of the best set of values compared to other reported values for $Na_3V_2(PO_4)_2O_2F$-based cathodes. The outstanding electrochemical performance of NVPF@C cathode material in Na^+/Li^+ storage batteries is related to the advantages of the favorable hierarchical mulberry-shaped architecture. (a) Nanosized primary particles effectively shorten ions diffusion distance in the crystal and expand the electrode-electrolyte

contact area. (b) In the hierarchical configurations, the primary nanoparticles building blocks could effectively avoid self-aggregation and structure degradation upon cycling. (c) The inter-particle pore network in the complex hierarchitectures could facilitate electrolyte penetration and simultaneously permit accommodation of large volume variation during charging-discharging processes. (d) The homogeneous *in-situ* carbon-coating layer establishes an electronic conduction network for fast electron transport between the $Na_3V_2(PO_4)_2O_2F$ nanoparticles, and the carbon layer can also help to mitigate strain effects caused by volume change during Na^+/Li^+ insertion/extraction processes, thereby improving cycle stability of the cathode.

CONCLUSIONS

In summary, we developed a rapid microwave-assisted low-temperature refluxing strategy to fabricate $Na_3V_2(PO_4)_2O_2F$@C material with an unique hierarchical mulberry-shaped self-assembly architecture. The $Na_3V_2(PO_4)_2O_2F$@C materials could serve as high performance cathodes for Na^+/Li^+ storage batteries with high operating plateaus (4.02 & 3.65 V *vs.* Na^+/Na, and 4.24 & 3.84 V *vs.* Li^+/Li), outstanding rate capabilities and excellent cycling stability. The excellent electrochemical properties of the NVPF@C electrode could be attributed to the fast ion/e^- transfer and negligible structural variation of the unique hierarchical self-assembled nanocomposites during the charge and discharge processes. Notably, the rapid and facile synthesis strategy to prepare hierarchical mulberry-shaped $Na_3V_2(PO_4)_2O_2F$@C can provide a new opportunity for the development of high-performance electrode materials for the energy storage systems.

Received 20 July 2018; accepted 20 August 2018; published online 8 October 2018

1 Nayak PK, Yang L, Brehm W, *et al.* From lithium-ion to sodium-ion batteries: advantages, challenges, and surprises. Angew Chem Int Ed, 2017, 57: 102–120
2 Ni Q, Bai Y, Wu F, *et al.* Polyanion-type electrode materials for sodium-ion batteries. Adv Sci, 2017, 4: 1600275
3 Wang D, Bie X, Fu Q, *et al.* Sodium vanadium titanium phosphate electrode for symmetric sodium-ion batteries with high power and long lifespan. Nat Commun, 2017, 8: 15888
4 You Y, Manthiram A. Progress in high-voltage cathode materials for rechargeable sodium-ion batteries. Adv Energy Mater, 2018, 8: 1701785
5 Masquelier C, Croguennec L. Polyanionic (phosphates, silicates, sulfates) frameworks as electrode materials for rechargeable Li (or Na) batteries. Chem Rev, 2013, 113: 6552–6591
6 Wang D, Chen N, Li M, *et al.* $Na_3V_2(PO_4)_3$/C composite as the intercalation-type anode material for sodium-ion batteries with superior rate capability and long-cycle life. J Mater Chem A, 2015, 3: 8636–8642
7 Zhu C, Wu C, Chen CC, *et al.* A high power–high energy $Na_3V_2(PO_4)_2F_3$ sodium cathode: investigation of transport parameters, rational design and realization. Chem Mater, 2017, 29: 5207–5215
8 Kawabe Y, Yabuuchi N, Kajiyama M, *et al.* Synthesis and electrode performance of carbon coated Na_2FePO_4F for rechargeable Na batteries. Electrochem Commun, 2011, 13: 1225–1228
9 Langrock A, Xu Y, Liu Y, *et al.* Carbon coated hollow Na_2FePO_4F spheres for Na-ion battery cathodes. J Power Sources, 2013, 223: 62–67
10 Deng X, Shi W, Sunarso J, *et al.* A green route to a Na_2FePO_4F-based cathode for sodium ion batteries of high rate and long cycling life. ACS Appl Mater Interfaces, 2017, 9: 16280–16287
11 Barker J, Saidi MY, Swoyer JL. A comparative investigation of the Li insertion properties of the novel fluorophosphate phases, $NaVPO_4F$ and $LiVPO_4F$. J Electrochem Soc, 2004, 151: A1670
12 Zhao J, He J, Ding X, *et al.* A novel sol–gel synthesis route to $NaVPO_4F$ as cathode material for hybrid lithium ion batteries. J Power Sources, 2010, 195: 6854–6859
13 Serras P, Palomares V, Goñi A, *et al.* High voltage cathode materials for Na-ion batteries of general formula $Na_3V_2O_{2x}(PO_4)_2F_{3-2x}$. J Mater Chem, 2012, 22: 22301
14 Serras P, Palomares V, Rojo T, *et al.* Structural evolution of high energy density V^{3+}/V^{4+} mixed valent $Na_3V_2O_{2x}(PO_4)_2F_{3-2x}$ (x=0.8) sodium vanadium fluorophosphate using *in situ* synchrotron X-ray powder diffraction. J Mater Chem A, 2014, 2: 7766–7779
15 Kumar PR, Jung YH, Lim CH, *et al.* $Na_3V_2O_{2x}(PO_4)_2F_{3-2x}$: a stable and high-voltage cathode material for aqueous sodium-ion batteries with high energy density. J Mater Chem A, 2015, 3: 6271–6275
16 Park YU, Seo DH, Kim H, *et al.* A family of high-performance cathode materials for Na-ion batteries, $Na_3(VO_{1-x}PO_4)_2F_{1+2x}$ ($0\le x\le 1$): combined first-principles and experimental study. Adv Funct Mater, 2014, 24: 4603–4614
17 Park YU, Seo DH, Kwon HS, *et al.* A new high-energy cathode for a Na-ion battery with ultrahigh stability. J Am Chem Soc, 2013, 135: 13870–13878
18 Deng G, Chao D, Guo Y, *et al.* Graphene quantum dots-shielded $Na_3(VO)_2(PO_4)_2F$@C nanocuboids as robust cathode for Na-ion battery. Energy Storage Mater, 2016, 5: 198–204
19 Qi Y, Mu L, Zhao J, *et al.* Superior Na-storage performance of low-temperature-synthesized $Na_3(VO_{1-x}PO_4)_2F_{1+2x}$ ($0\le x\le 1$) nanoparticles for Na-ion batteries. Angew Chem Int Ed, 2015, 54: 9911–9916
20 Sauvage F, Quarez E, Tarascon JM, *et al.* Crystal structure and electrochemical properties *vs.* Na^+ of the sodium fluorophosphate $Na_{1.5}VOPO_4F_{0.5}$. Solid State Sci, 2006, 8: 1215–1221
21 Guo JZ, Wang PF, Wu XL, *et al.* High-energy/power and low-temperature cathode for sodium-ion batteries: *in situ* XRD study and superior full-cell performance. Adv Mater, 2017, 29: 1701968
22 Chao D, Lai CHM, Liang P, *et al.* Sodium vanadium fluorophosphates (NVOPF) array cathode designed for high-rate full sodium ion storage device. Adv Energy Mater, 2018, 8: 1800058
23 Jin H, Liu M, Uchaker E, *et al.* Nanoporous carbon leading to the high performance of a $Na_3V_2O_2(PO_4)_2F$@carbon/graphene cathode in a sodium ion battery. CrystEngComm, 2017, 19: 4287–4293

24 Zhao J, Yang X, Yao Y, *et al.* Moving to aqueous binder: a valid approach to achieving high-rate capability and long-term durability for sodium-ion battery. Adv Sci, 2018, 5: 1700768
25 Zan G, Wu Q. Biomimetic and bioinspired synthesis of nanomaterials/nanostructures. Adv Mater, 2016, 28: 2099–2147
26 Baghbanzadeh M, Carbone L, Cozzoli PD, *et al.* Microwave-assisted synthesis of colloidal inorganic nanocrystals. Angew Chem Int Ed, 2011, 50: 11312–11359
27 Wang D, Liu Q, Chen C, *et al.* Nasicon-structured $NaTi_2(PO_4)_3$@C nanocomposite as the low operation-voltage anode material for high-performance sodium-ion batteries. ACS Appl Mater Interfaces, 2016, 8: 2238–2246
28 Xu M, Wang L, Zhao X, *et al.* $Na_3V_2O_2(PO_4)_2F$/graphene sandwich structure for high-performance cathode of a sodium-ion battery. Phys Chem Chem Phys, 2013, 15: 13032–13037
29 Hou Y, Chang K, Li B, *et al.* Highly [010]-oriented self-assembled $LiCoPO_4$/C nanoflakes as high-performance cathode for lithium ion batteries. Nano Res, 2018, 11: 2424–2435
30 Zheng YZ, Ding H, Uchaker E, *et al.* Nickel-mediated polyol synthesis of hierarchical V_2O_5 hollow microspheres with enhanced lithium storage properties. J Mater Chem A, 2015, 3: 1979–1985
31 Wu S, Zhu Y, Huo Y, *et al.* Bimetallic organic frameworks derived CuNi/carbon nanocomposites as efficient electrocatalysts for oxygen reduction reaction. Sci China Mater, 2017, 60: 654–663
32 Massa W, Yakubovich OV, Dimitrova OV. Crystal structure of a new sodium vanadyl(IV) fluoride phosphate $Na_3\{V_2O_2F[PO_4]_2\}$. Solid State Sci, 2002, 4: 495–501
33 Jin H, Dong J, Uchaker E, *et al.* Three dimensional architecture of carbon wrapped multilayer $Na_3V_2O_2(PO_4)_2F$ nanocubes embedded in graphene for improved sodium ion batteries. J Mater Chem A, 2015, 3: 17563–17568
34 Harrison KL, Manthiram A. Microwave-assisted solvothermal synthesis and characterization of metastable $LiFe_{1-x}(VO)_xPO_4$ cathodes. Inorg Chem, 2011, 50: 3613–3620
35 Saravanan K, Mason CW, Rudola A, *et al.* The first report on excellent cycling stability and superior rate capability of $Na_3V_2(PO_4)_3$ for sodium ion batteries. Adv Energy Mater, 2013, 3: 444–450
36 Serras P, Palomares V, Alonso J, *et al.* Electrochemical Na extraction/insertion of $Na_3V_2O_{2x}(PO_4)_2F_{3-2x}$. Chem Mater, 2013, 25: 4917–4925
37 Yin Y, Xiong F, Pei C, *et al.* Robust three-dimensional graphene skeleton encapsulated $Na_3V_2O_2(PO_4)_2F$ nanoparticles as a high-rate and long-life cathode of sodium-ion batteries. Nano Energy, 2017, 41: 452–459
38 Yang T, Qian T, Wang M, *et al.* A sustainable route from biomass byproduct okara to high content nitrogen-doped carbon sheets for efficient sodium ion batteries. Adv Mater, 2016, 28: 539–545
39 Ni Q, Bai Y, Li Y, *et al.* 3D electronic channels wrapped large-sized $Na_3V_2(PO_4)_3$ as flexible electrode for sodium-ion batteries. Small, 2018, 327: 1702864
40 Guo JZ, Yang Y, Liu DS, *et al.* A practicable Li/Na-ion hybrid full battery assembled by a high-voltage cathode and commercial graphite anode: superior energy storage performance and working mechanism. Adv Energy Mater, 2018, 8: 1702504
41 An Q, Xiong F, Wei Q, *et al.* Nanoflake-assembled hierarchical $Na_3V_2(PO_4)_3$/C microflowers: Superior Li storage performance and insertion/extraction mechanism. Adv Energy Mater, 2015, 5: 1401963
42 Wu S, Wang W, Li M, *et al.* Highly durable organic electrode for sodium-ion batteries *via* a stabilized α-C radical intermediate. Nat Commun, 2016, 7: 13318

Acknowledgements This work was supported by the National Natural Science Foundation of China (21303042, 21875097, 21671096 and 21603094), Guangdong Special Support for the Science and Technology Leading Young Scientist (2016TQ03C919), and the Basic Research Project of the Science and Technology Innovation Commission of Shenzhen (JCYJ20170412153139454 and JCYJ20170817110251498).

Author contributions Hou Y performed the experiments and wrote the manuscript with the guidance from Lu Z and Chang Z. All authors contributed to the general discussion and revision.

Conflict of interest The authors declare that they have no conflict of interest.

Supplementary information Supporting information is available in the online version of the paper.

Yan Hou is a PhD student at Henan Normal University. Her research focuses on the development of high-voltage cathode materials for lithium/sodium ion batteries.

Zhouguang Lu is now a Professor in the Department of Materials Science and Engineering, South University of Science and Technology of China. He obtained his BSc from the Central South University in 2001, his MSc degree, under the joint master program between Tsinghua University and Central South University in 2004, and PhD from the City University of Hong Kong in 2009. He is the recipient of Fulbright Fellowship of USA Government in 2008-2009 and the Overseas High-Caliber Personnel (Level B) of Shenzhen Government in 2013. His research mainly covers the design and synthesis of nanostructures and their application in energy storage and conversion with focus on lithium/sodium ion batteries, and lithium-air batteries. He has authored more than 100 peer-review journal papers with total citations of more than 4000 and h-index of 38.

微波辅助回流法制备桑椹形$Na_3V_2(PO_4)_2O_2F$@C正极材料用于高性能钠/锂离子电池

侯燕[1,2], 常焜[3], 王振宇[2], 顾帅[2], 刘琼[2], 张钧君[2], 程化[2], 张圣麟[1], 常照荣[1*], 卢周广[2*]

摘要 本论文采用快速微波辅助低温回流策略制备了桑椹形$Na_3V_2(PO_4)_2O_2F$@C纳米复合材料. 研究表明微乳液中的$V(acac)_3$反胶束体系对该自组装结构的形成起到了关键作用. 制得的$Na_3V_2(PO_4)_2O_2F$晶粒沿着[002]方向生长并被原位包封在碳壳中, 形成了高度稳定的自组装结构, 这不仅有利于Na^+/e^-的快速迁移, 而且能够有效改善电极材料的循环性能并抑制电压衰减. 作为钠离子电池正极材料, 在0.1 C条件下, $Na_3V_2(PO_4)_2O_2F$@C的初始放电容量约为127.9 mA h g^{-1}. 在高倍率(20 C)条件下, 容量达88.1 mA h g^{-1}, 2000次循环后容量保持率为82.1%. 此外, 利用非原位X射线衍射, X射线光电子能谱和恒电流间歇滴定技术, 初步研究了$Na_3V_2(PO_4)_2O_2F$@C在充放电过程中的反应机理和Na^+迁移机制. 同时, 在Li/Na离子混合电池当中, $Na_3V_2(PO_4)_2O_2F$@C也表现出了优异的倍率和循环性能. 上述微波辅助低温回流合成策略为开发高性能电化学储能材料开辟了新的途径.

